Sintering of W-substituted Na_3SbS_4 Electrolytes: Effect of Phase Composition, Voids, and Interface Contact

Fuwei Wen, Xiang You, Geng Xie, Arthur Mar, and Lingzi Sang*

Department of Chemistry, University of Alberta, Edmonton, Alberta T6G 2G2, Canada

*Corresponding Author: Lingzi Sang, lsang@ualberta.ca

Table of Contents

Figure S8. *RC circuit model used to analyze the EIS data obtained from the Na/WNSS/Na cells and extract the evolution of interfacial resistance. In this model R2/Q2 represent the contribution from WNSS bulk resistance, and R3/Q3 reflect the interfacial component, where the magnitude of R3 was used as* R_{int}.

Table S3. *Interface resistance and capacitance of Na/WNSS/Na cells during cycling*

Figure S9. *Cyclic voltammetry results obtained from Na/WNSS-16/Na cells assembled using (A) as-synthesized and (B) sintered WNSS.*

Figure S10. *EIS results obtained from Na/WNSS-16/Na cells before and after the first five CV cycles. Cells were assembled using (A) as-synthesized and (B) sintered WNSS.*

Figure S11. *2p XPS spectra obtained from (A) as-synthesized WNSS-16 powder, (B) sintered and regrinded WNSS-16 powder, (C) sintered WNSS-16 pellet surface, (D) as-synthesized and cycled WNSS-pellet, (E) Na electrode disassembled from Na/WNSS-16/Na cell following charge/discharge cycles.*

Figure S12. *Sb 3d XPS spectra obtained from (A) as-synthesized WNSS-16 powder, (B) sintered and regrinded WNSS-16 powder, (C) sintered WNSS-16 pellet surface, (D) as-synthesized and cycled WNSS-pellet, (E) Na electrode disassembled from Na/WNSS-16/Na cell following charge/discharge cycles.*

Experimental Section

Preparation of As-synthesized and Sintered WNSS Samples

$Na_{3-x}Sb_{1-x}W_xS_4$ (WNSS, x = 0.12, 0.16, 0.24, 0.32) were prepared by mixing stochiometric amounts of Na_2S (Sigma-Aldrich, 98%), WS_2 (Sigma-Aldrich, 99%), Sb_2S_3 (Onyxmet, >90%), and S (Anachemia Chemicals, >90%) powders. A 5 mol% excess of S was added to compensate for the volatilized losses during synthesis. Nominal compositions are reported throughout this work. Each resulting mixture, with a total mass of 250 mg, was pressed into a pellet that was 1/4 in. (6.35 mm) in diameter. The pellet was loaded into an evacuated (< 10^{-6} Torr) fused-silica ampule (7 mm inner diameter) and placed in a tube furnace (Lindberg/Blue M Mini-Mite, ThermoFisher Scientific). The temperature profile was programmed for a 17 h heating ramp from room temperature to 550 °C (~30 °C/h), followed by holding at 550 °C for 48 h before cooling back down to room temperature over a period of 10 h. The resulting pellet was reground in an agate mortar for 2 min in an Ar-filled glove box and used as the as-prepared WNSS powder.

Sintered samples were prepared by pelletizing 86-89 mg of as-prepared WNSS powders into a 1/4 in. (6.35 mm) diameter pellet at 464 MPa (1.5 metric tons) inside an Ar-filled glove box. The resulting pellet thickness is 1 mm (± 0.1 mm). The pellet was loaded into an evacuated (< 10^{-6} Torr) fused-silica ampule (10 mm inner diameter) and placed in a tube furnace (Lindberg/Blue M Mini-Mite, ThermoFisher Scientific) for a post-synthesis sintering process. The temperature profile was programmed for a 17 h heating ramp from room temperature to 500 °C (~30 °C/h), followed by holding at 500 °C for 48 h before cooling back down to room temperature over a period of 10 h.

Powder X-ray Diffraction (XRD)

Powder XRD patterns were collected on a Bruker D8 Advance instrument with a Cu Kα source at 40 kV and 40 mA. All patterns were collected in 1D mode with 2θ range from 5 to 90 degrees over 80 min, in steps of 0.02 degrees and 1 s per step. The samples were protected under an Ar atmosphere by encapsulating the powders using polyimide tape (CGSTAPE-8258).

Raman Spectroscopy

WNSS samples (powders or pellet fragments) for Raman measurements were placed on a glass microscope slide and encapsulated using a polyimide tape (CGSTAPE-8258) to protect them from air exposure. A 532 nm (50 mW) laser excitation source was used in Raman analysis. Raman spectra were collected using two Raman instruments: a Renishaw inVia Qontor confocal Raman microscope equipped with a 50× magnification objective lens (~1.3 μm beam diameter at the sample) and a custom-built benchtop Raman spectrometer equipped with an ANDOR Solis DU-970N CCD (~50 μm beam diameter at the sample). Large beam Raman provides an overview of powder or pellet surface, whereas small beam Raman provides a detailed view of localized positions. Raman spectra between 100 cm^{-1} and 1136 cm^{-1} were acquired over 60 s.

Plasma Focused Ion Beam Scanning Electron Microscopy (PFIB-SEM)

PFIB-SEM images were acquired using a ThermoFisher Helios 5 Hydra Dual Beam system. The WNSS sample pellets before and after sintering as described above were affixed with carbon tape onto an aluminum stage. Pellet surfaces were covered by a 1.2

μm carbon layer and a 2.5 μm thick tungsten layer sequentially to protect the sample surface from being damaged during ion milling. Specifically, a 200 nm thick layer of C was first deposited via electron beam deposition (5 kV and 13 nA), followed by a 1 μm thick layer of C deposited with an ion beam (12 kV and 2.5 nA) to cover the area of interest on the sample surface. Next, a 2.5 μm thick layer of W was deposited on top of the carbon layer. For milling and cross-section characterization, a trench with dimensions of 10 μm × 15 μm × 4 μm was created by rough ion milling at 30 kV and 4 nA. Fine polishing of the pellet cross-section was accomplished stepwise with each step milling a small area (10 μm × 1 μm × 4 μm) at the pellet cross-section. To avoid surface damage of the samples, low power (30 kV and 0.3 nA) was used during polishing. The polished cross-sections of the sample were imaged and analyzed following every polishing step.

Electrochemical Characterization

Ionic conductivity of WNSS was measured on as-prepared WNSS powders, sintered pellets, and powders harvested from regrinding the sintered pellet. For each as-prepared sample, 86-69 mg of powder was loaded into the die set and pressed at 464 MPa (1.5 Metric Tons) pressure. Then the die was inserted into the air-tight EIS measurement cell for PEIS measurements. For each sintered pellet, the impedance was measured by directly sandwiching the pellet between steel plungers in the measurement die body. For powders obtained from sintered pellet, a sintered pellet was reground in an agate mortar for 2 min in an Ar-filled glove box and re-pelletized following the same conditions as the as-synthesized samples.

Galvanostatic charge/discharge experiments were performed in a Swagelok cell. To prepare Na/WNSS/Na symmetric cells, Na plates were placed on both sides of the WNSS pellets before hand-pressing the three-layer samples in a Swadgelok cell. All cell assembling and charge/discharge measurements were conducted at room temperature. The measurement consisted of an initial resting period at open circuit voltage of the cell for 10 seconds, oxidation and reduction cycles, followed by potentiostatic electrochemical impedance spectroscopy (PEIS) from 7 MHz to 1 Hz with a logarithmic spacing of 30 points per decade. Each data point collected was an average of 2 measurements. Anodic and cathodic current segments at a 0.10 $mA \cdot cm^{-2}$ magnitude were applied for 1 hour each. A total of 12 oxidation and reduction cycles were applied.

Cyclic voltammetry was conducted for a Na/WNSS-16/Na symmetric cell. Potential sweeps between ± 0.1 V (vs Na/Na^{+}) were performed for 5 cycles at a 0.1 mV/sec sweep rate. EIS data were collected before CV and after each cycle using the same parameters as discussed in the galvanostatic charge/discharge experiments.

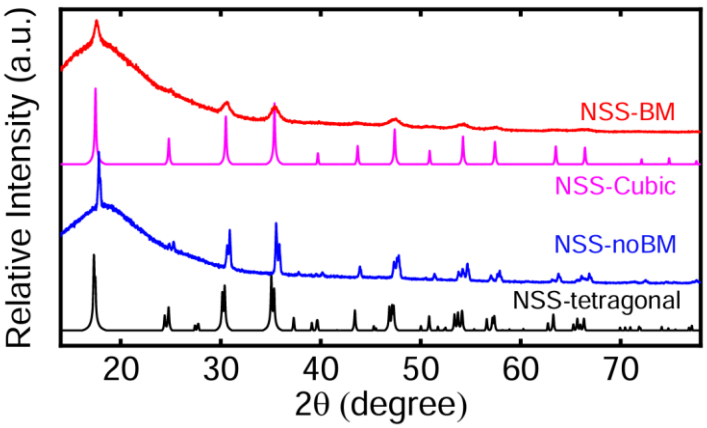

Figure S1. *Powder XRD patterns obtained from powdered Na_3SbS_4-noBM and -BM compounds compared to simulated diffraction patterns for tetragonal and cubic Na_3SbS_4. Figure reproduced from reference 1, with the permission of American Chemical Society, 2023.*

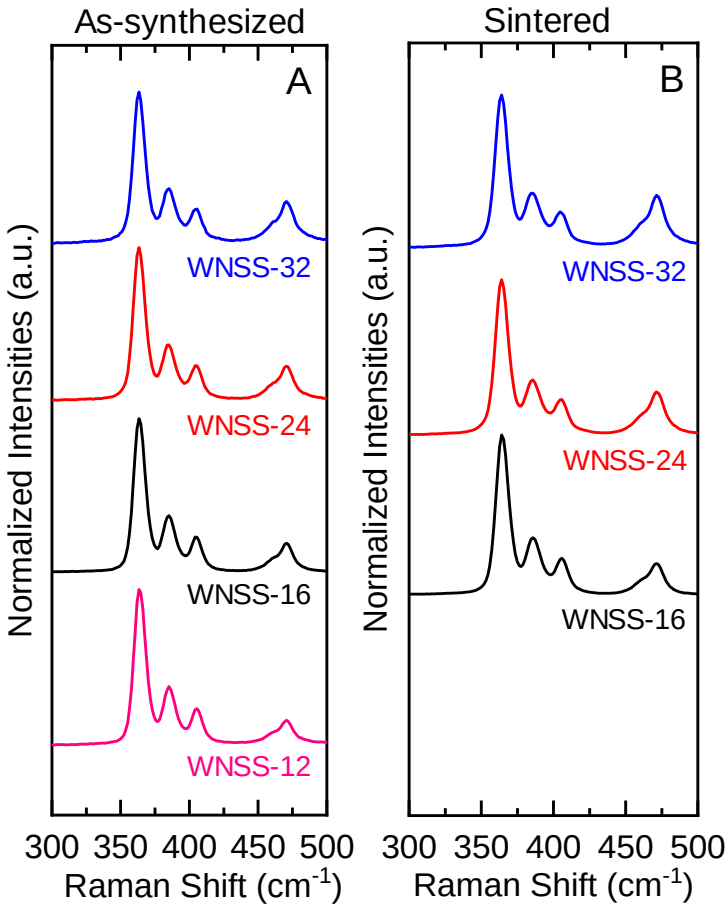

Figure S2. *Raman spectra obtained from (A) as-prepared and (B) sintered WNSS powders. Laser beam size ≈ 50 μm diameter.*

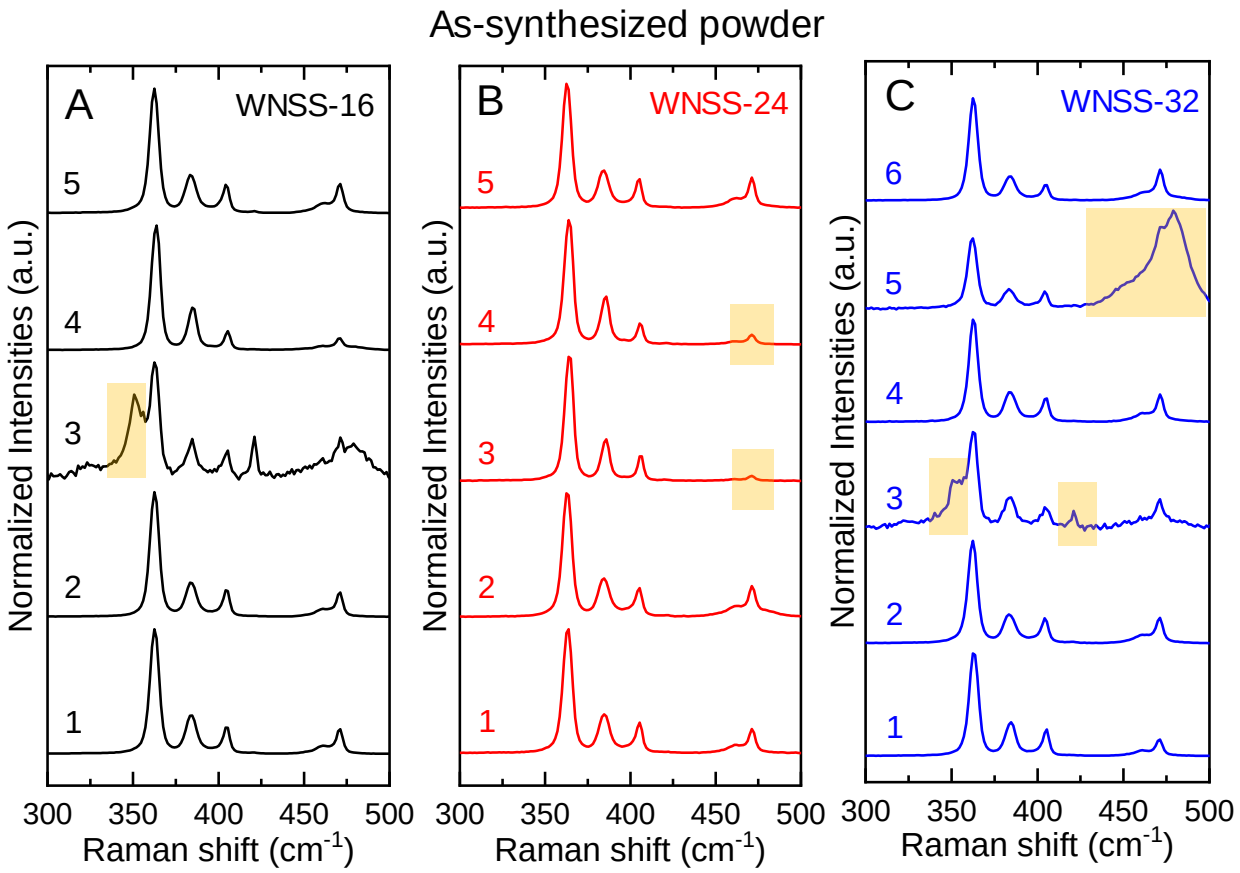

***Figure S3**. Raman spectra obtained from randomly picked local spots on the as-prepared powders of (A) WNSS-16, (B) WNSS-24, and (C) WNSS-32. Vibrational modes of secondary phases are highlighted. Laser beam size ≈ 1.3 μm diameter*

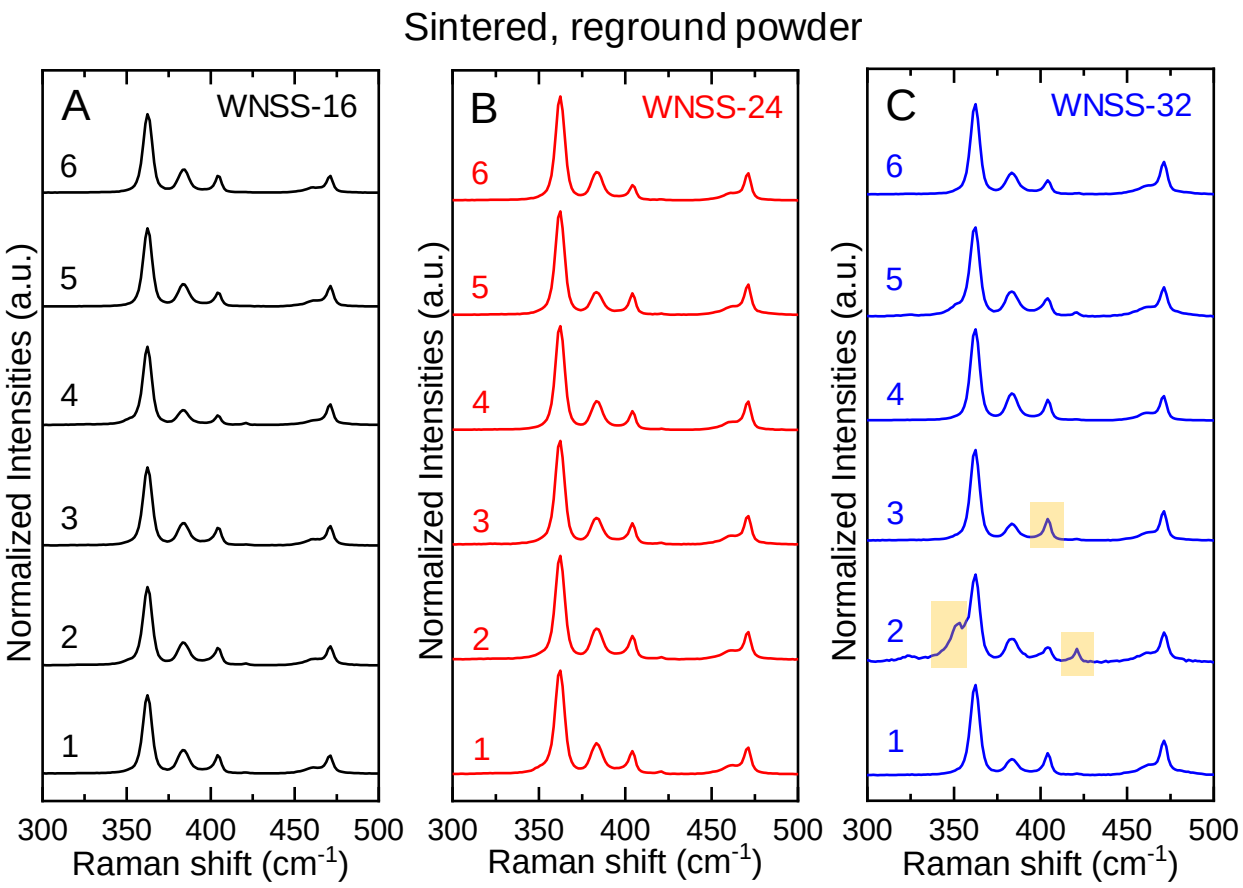

Figure S4. *Raman spectra obtained from randomly picked local spots on the sintered and reground powders of (A) WNSS-16, (B) WNSS-24, and (C) WNSS-32. Vibrational modes of secondary phases are highlighted. Laser beam size ≈ 1.3 μm diameter*

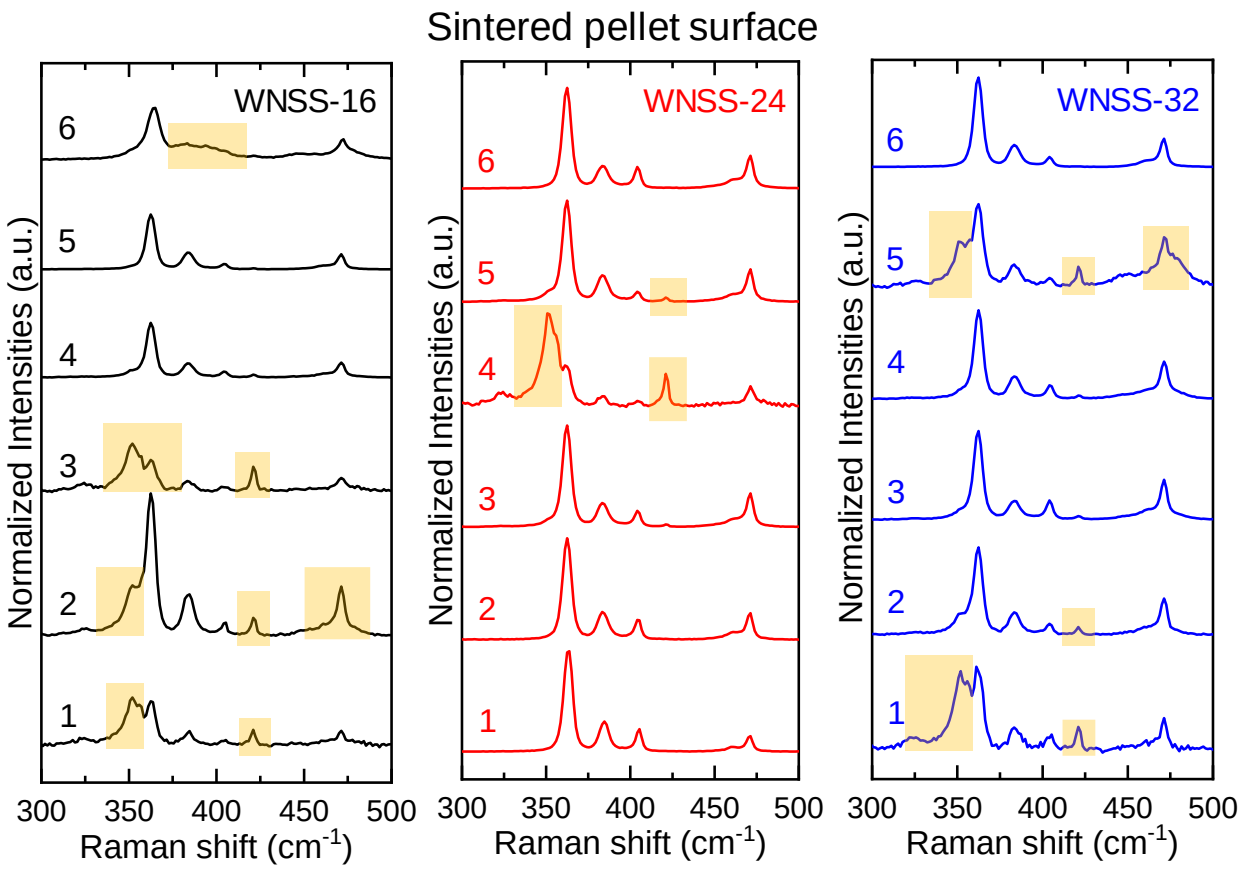

Figure S5. *Raman spectra obtained from randomly picked local spots on the sintered pellet surface of (A) WNSS-16, (B) WNSS-24, and (C) WNSS-32. Vibrational modes of secondary phases are highlighted. Laser beam size ≈ 1.3 μm diameter.*

<u>Na^+ conductivity measurements from C/WNSS/C blocking cell.</u>

EIS measurement from C/WNSS/C blocking cell was conducted on WNSS-16, -24, -32 samples before and after sintering. **Figure S5** shows the obtained Nquist plots. Dimensions of all samples were controlled to exhibit a 1/4 –inch diameter and ~1 mm thickness. This is done by precisely controlling the mass loading for each measurement to ensure WNSS loaded weights between 85.5 – 87.0 mg. The Nyquist plots were further analyzed by model fitting using the previously described RC circuit shown in **Figure S6**.[2-4] Specifically, parallel components R2 and Q2 represent the resistor and constant phase element within the WNSS solid electrolyte pellet, while R1 represents resistive components in the circuit loop other than the contribution from the solid-electrolyte. Note that contribution from grain boundary resistivity may be present in this system, which should presumably be responsible for a distinct semicircle. A well-resolved semicircle component is not shown in our experimentally obtained Nyquist plot, and therefore cannot be deconvoluted. As a result, we consider R2 as the overall

resistance of the solid-state electrolyte. One calculation example is shown below to provide details about obtaining Na^+ conductivity from the model fitting results.

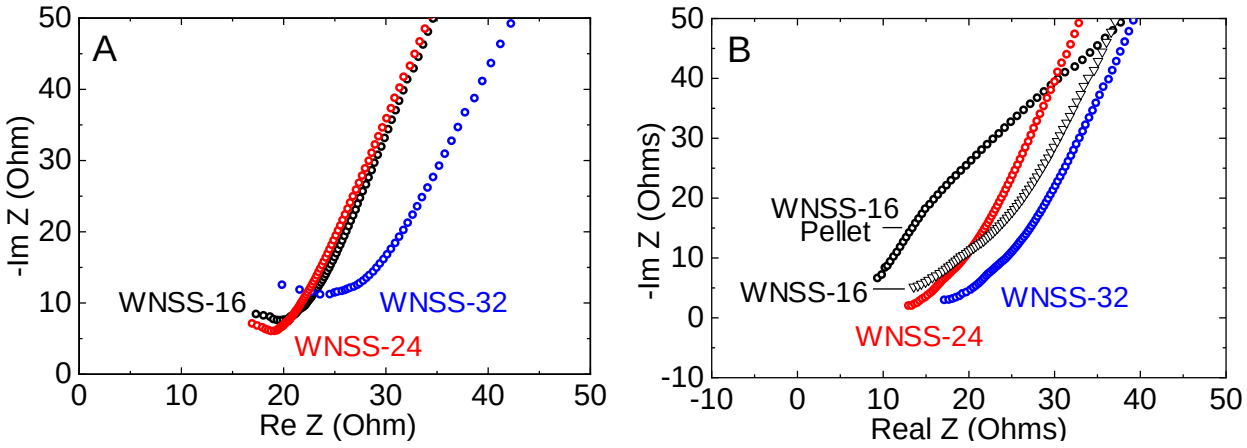

Figure S6. *Examples of EIS obtained from C/WNSS/C cells for (A) as-synthesized WNSS power, (B) sintered and regrinded WNSS powder. Measurements were made using an impedance die at ¼-inch diameter. Powders were compressed to ~1 mm thickness in the impedance die. EIS data of the "WNSS-16 pellet" were obtained from a sintered pellet before regrinding.*

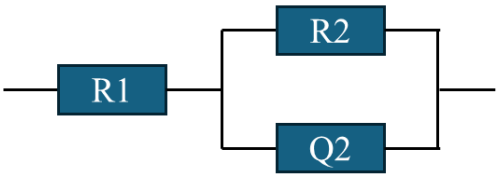

Figure S7. *RC circuit model used to analyze the EIS data and extract ionic conductivity of WNSS samples.*

Using the Nyquist plot obtained from an as-synthesized WNSS-16 sample as an example, model fitting result suggests that R2 = 17.39 ± 0.86 Ω, R1 = 6.562 ± 1.477 Ω. We determined that the total resistance contributed by the WNSS pellet was ~17.4 ± 0.9 Ω. Following **Equation S1**

$$\sigma = \frac{l}{RA} \qquad \textbf{Equation S1}$$

Calculation Example:

$$\sigma = \frac{l}{RA} = \frac{0.1005\ cm}{17.4\ \Omega \times \pi \times (\frac{0.635\ cm}{2})^2} = 0.0182\ S/cm = 18.2\ mS/cm$$

Therefore, the calculated ionic conductivity for this sample is 18.2 mS/cm with ¼ inch (0.635 cm) diameter measurement die and 0.1005 cm pellet thickness. The uncertainty value for ionic conductivity is calculated by measuring multiple samples independently synthesized from different batches to ensure reproducibility in synthesis and sintering processing are considered.

Table S1. Na^+ conductivity obtained from WNSS samples

Sample Index	Na^+ conductivity ($mS \cdot cm^{-1}$)		
	As-synthesized powder	Sintered powder	Sintered Pellet
WNSS-12	16.7 ± 4.0	-	-
WNSS-16	18.0 ± 0.2	23.3 ± 2.2	34.1 ± 19.6
WNSS-24	21.2 ± 0.9	61.9 ± 10.5	-
WNSS-32	12.9 ± 1.5	43.4 ± 3.4	-

Table S2. An example of Mass, dimension, and density of a WNSS-16 before and after sintering

	As-synthesized WNSS-16	Sintered WNSS-16
Diameter (D)	0.636 cm	0.630 cm
ΔD	±0.001 cm	±0.001 cm
Thickness (d)	0.1008 cm	0.1008 cm
Δd	±0.0001 cm	±0.0001 cm
Mass (m)	0.0855 g	0.0855 g
Δm	±0.0001 g	±0.0001 g
Density (ρ)	2.670 g/cm^3	2.721 g/cm^3
Δρ	±0.007 g/cm^3	±0.007 g/cm^3
ρ ± Δρ	2.663 – 2.677 g/cm^3	2.714 – 2.728 g/cm^3

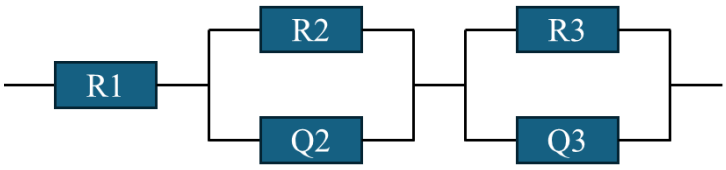

Figure S8. *RC circuit model used to analyze the EIS data obtained from the Na/WNSS/Na cells and extract the evolution of interfacial resistance. In this model R2/Q2 represent the contribution from WNSS bulk resistance, and R3/Q3 reflect the interfacial component, where the magnitude of R3 was used as* R_{int}.

Table S3. Interface resistance and capacitance of Na/WNSS/Na cells during cycling

Cycle number	As-synthesized WNSS-16		Sintered WNSS-16 pellet	
	R_{int} (kΩ)	Capacitance (μF)	R_{int} (kΩ)	Capacitance (μF)
Pre-cycling	0.834	1.53×10^{-3}	0.750	3.52×10^{-3}
12	20.0	1.85×10^{-4}	44.2	7.94×10^{-5}
24	26.1	1.56×10^{-4}	68.8	6.64×10^{-5}
36	30.9	1.26×10^{-4}	87.8	5.50×10^{-5}
48	32.8	1.10×10^{-4}	102.6	4.92×10^{-5}

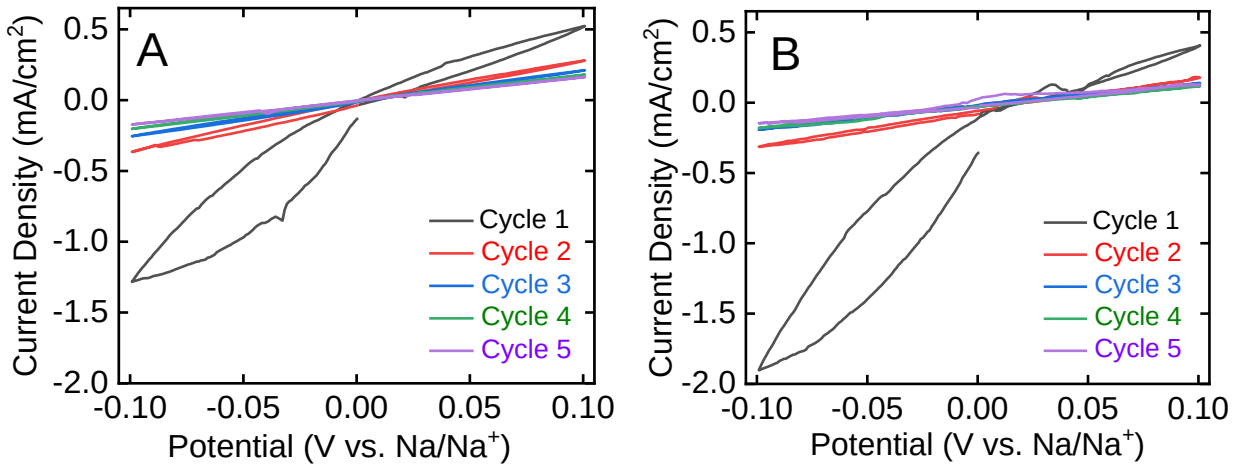

Figure S9. *Cyclic voltammetry results obtained from Na/WNSS-16/Na cells assembled using (A) as-synthesized and (B) sintered WNSS.*

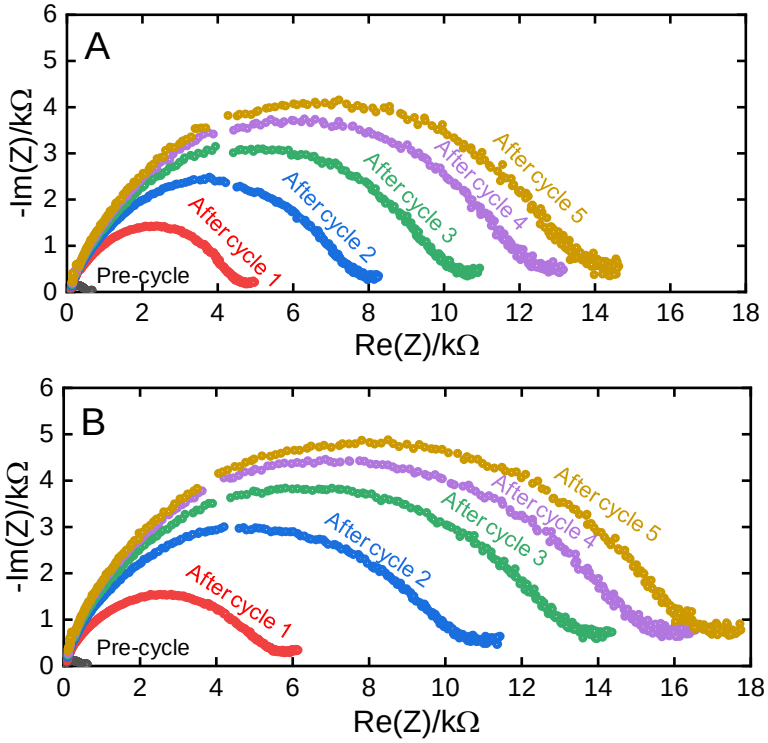

Figure S10. *EIS results obtained from Na/WNSS-16/Na cells before and after the first five CV cycles. Cells were assembled using (A) as-synthesized and (B) sintered WNSS.*

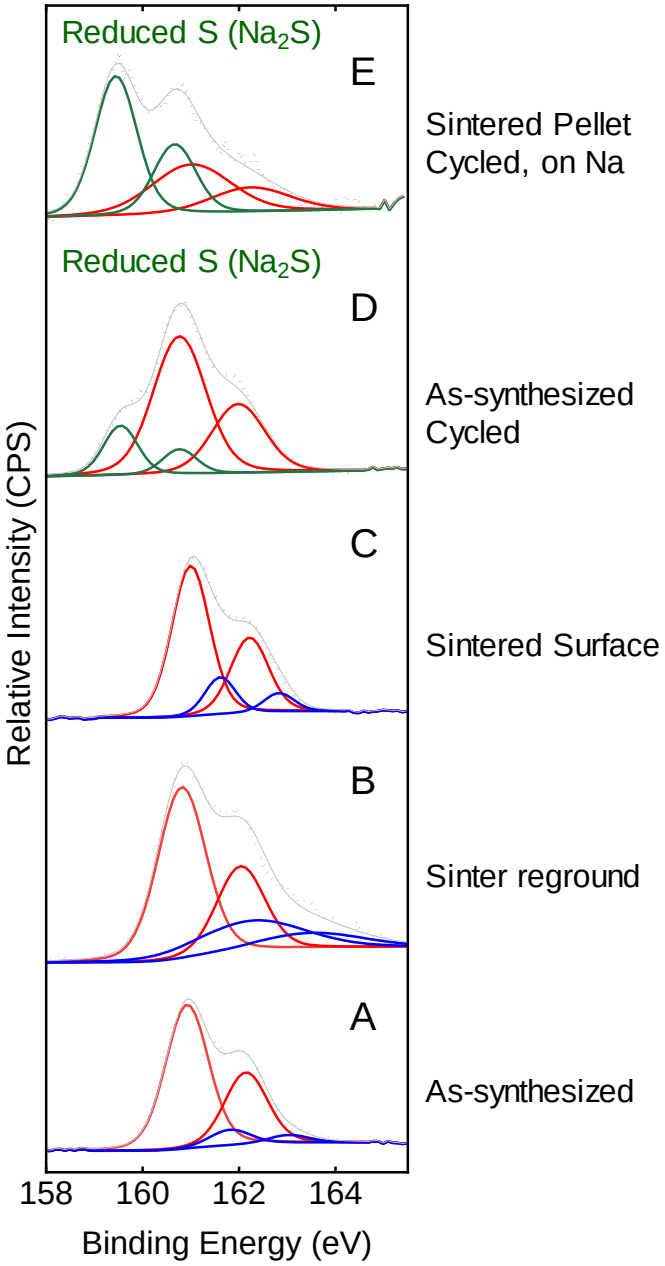

Figure S11. *2p XPS spectra obtained from (A) as-synthesized WNSS-16 powder, (B) sintered and regrinded WNSS-16 powder, (C) sintered WNSS-16 pellet surface, (D) as-synthesized and cycled WNSS-pellet, (E) Na electrode disassembled from Na/WNSS-16/Na cell following charge/discharge cycles.*

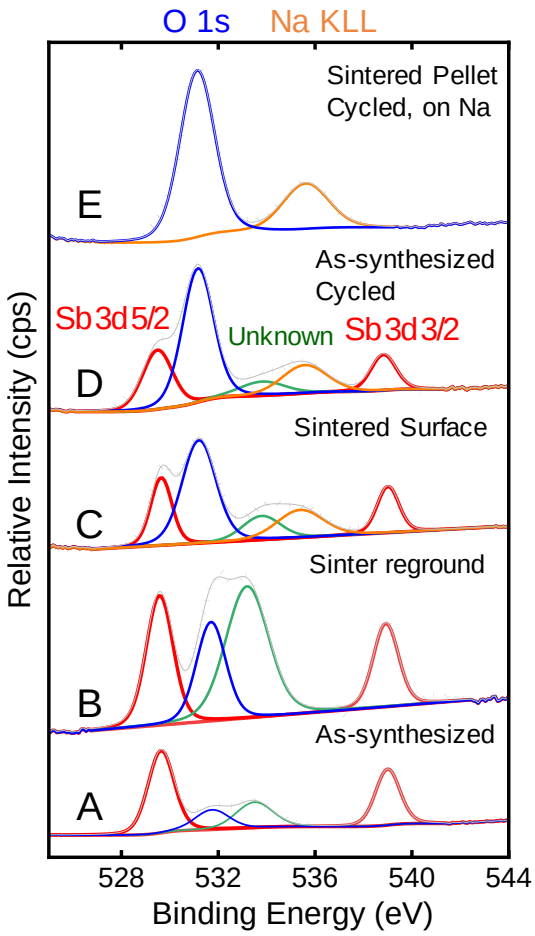

Figure S12. *Sb 3d XPS spectra obtained from (A) as-synthesized WNSS-16 powder, (B) sintered and regrinded WNSS-16 powder, (C) sintered WNSS-16 pellet surface, (D) as-synthesized and cycled WNSS-pellet, (E) Na electrode disassembled from Na/WNSS-16/Na cell following charge/discharge cycles.*

References

1. Wen, F.; Xie, G.; Chen, N.; Wu, Q.; Chaudhary, M.; You, X.; Michaelis, V. M.; Mar, A.; and Sang, L.; Mechanochemistry in Sodium Thioantimonate Solid Electrolytes: Effects on Structure, Morphology, and Electrochemical Performance ACS Appl. Mater. Interfaces, 2023,15,40070−40079.

2. Zhang, S. M.; Zhao, F. P.; Wang, S.; Liang, J. W.; Wang, J.; Wang, C. H.; Zhang, H.; Adair, K.; Li, W. H.; Li, M. S.; Duan, H.; Zhao, Y.; Yu, R. Z.; Li, R. Y.; Huang, H.; Zhang, L.; Zhao, S. Q.; Lu, S. G.; Sham, T. K.; Mo, Y. F.; Sun, X. L., Advanced High-Voltage All-Solid-State Li-Ion Batteries Enabled by a Dual-Halogen Solid Electrolyte. Adv. Energy Mater. ***2021,*** *11, 2100836.*

3. Rosa, C.; Ravalli, M.; Pianta, N.; Mustarelli, P.; Ferrara, C.; Quartarone, E.; Malavasi, L.; Sheptyakov, D.; Tealdi, C., Aliovalent Substitution in Li3InCl6: A Combined Experimental and Computational Investigation of Structure and Ion Diffusion in Lithium-Halide Solid State Electrolytes. ACS Appl. Energy Mater. ***2024,*** *7, 4314-4323.*

4. Luo, X.; Hu, X.; Zhong, Y.; Wang, X.; Tu, J., Degradation Evolution for Li2ZrCl6 Electrolytes in Humid Air and Enhanced Air Stability via Effective Indium Substitution. Small ***2024,*** *20, e2306736.*